

This is the author's peer reviewed, accepted manuscript. However, the online version of record will be different from this version once it has been copyedited and typeset.

PLEASE CITE THIS ARTICLE AS DOI: 10.1063/5.0008867

## Terahertz quantum-cascade patch-antenna VECSEL with low power dissipation

Christopher A. Curwen,<sup>1</sup> John L. Reno,<sup>2</sup> and Benjamin S. Williams<sup>1</sup>

<sup>1</sup>*Department of Electrical and Computer Engineering, University of California, Los Angeles, California 90095, USA*

<sup>2</sup>*Sandia National Laboratories, Center of Integrated Nanotechnologies, MS 1303, Albuquerque, New Mexico 87185, USA*

We report a terahertz quantum-cascade vertical-external-cavity surface-emitting laser (QC-VECSEL) based upon a metasurface consisting of an array of gain-loaded resonant patch antennas. Compared with the typical ridge-based metasurfaces previously used for QC-VECSELs, the patch antenna surface can be designed with a much sparser fill factor of gain material, which allows for reduced heat dissipation and improved thermal performance. It also exhibits larger amplification thanks to enhanced interaction between the incident radiation and the QC-gain material. We demonstrate devices that produce several milliwatts of continuous-wave power in a single mode at  $\sim$ 4.6 THz, and dissipate less than 1 W of pump power. Use of different output couplers demonstrates the ability to optimize device performance for either high power, or high operating temperature. Maximum demonstrated power is 6.7 mW at 4 K (0.67% wall-plug efficiency (WPE)), and 0.8 mW at 77 K (0.06% WPE). Directive output beams are measured throughout with divergence angles of  $\sim$ 5°.

### THE MANUSCRIPT

The terahertz (THz) quantum-cascade (QC) vertical-external-cavity surface-emitting laser (VECSEL) is a recently developed approach for designing THz QC-lasers with scalable output power and high-quality beam patterns.<sup>1</sup> The enabling component of the QC-VECSEL is an amplifying metasurface – a reflectarray of resonant antenna-coupled THz QC-gain elements with subwavelength spacing that exhibits a reflectance  $R$  greater than unity across some finite gain bandwidth. The antenna elements are unable to lase on their own due to high surface radiation losses, but instead, the metasurface is used as the amplifying element of an external cavity laser. The external cavity mode effectively phase locks the antenna elements, and because the metasurface can be made large relative to the lasing wavelength, near-diffraction-limited beams with high power have been observed.<sup>2</sup> The external-cavity allows one to more easily modify the outcoupling efficiency and cavity resonant frequency,<sup>3</sup> while the metasurface offers unique opportunities such as engineering of “flat-optics” focusing<sup>2</sup> and polarization switchability.<sup>4</sup> The typical metasurface design consists of a 1D sub-wavelength array of narrow metal-metal ridges of width  $w$  and period  $\Lambda$  that are coupled to surface radiation via the  $TM_{01}$  cutoff resonances of the ridges.<sup>5,6</sup> This design has been used to realize many high-performance VECSELs operating between 3-4 THz.<sup>3,7,8</sup>

This is the author's peer reviewed, accepted manuscript. However, the online version of record will be different from this version once it has been copyedited and typeset.

PLEASE CITE THIS ARTICLE AS DOI: 10.1063/5.0008867

In this Letter we report a QC-VECSEL using an amplifying patch-antenna based metasurface. Patch resonators support a transverse half-wavelength resonance, and can be considered shorter versions of the previously mentioned ridge antennas.<sup>9,10</sup> The integration of intersubband material with patch antenna arrays has been an interesting field of research because intersubband devices operate in the THz and mid-infrared (mid-IR) frequency ranges, where metallic antennas can be used to strongly confine the light to subwavelength scales without severe losses.<sup>11</sup> For example, the field enhancement in patch antenna arrays has been used to demonstrate strong coupling for intersubband polaritons and quantum-well infrared photodetectors with enhanced detectivity.<sup>12-14</sup> Conversely, patch antenna arrays have been used to achieve spontaneous emission enhancement (Purcell effect) from THz QC material,<sup>15</sup> and more recently to realize large-area surface emitting THz QC-lasers.<sup>16</sup> Here, we leverage this enhanced interaction to improve upon the THz QC-VECSEL by increasing the reflectance of the metasurface for a given quantity of intersubband gain while simultaneously reducing the VECSEL power dissipation.

The first advantage of the patch-based metasurface is related to its increased reflectance compared to a ridge-based metasurface with the same QC-material gain coefficient ( $g$ , in units  $\text{cm}^{-1}$ ). This becomes particularly useful as we scale our designs to higher frequencies (4.7 THz in this case). We can consider the free-standing metasurface as an open resonator, which exhibits a total quality factor  $Q$  that can be written  $Q^{-1}=Q_{\text{rad}}^{-1}+Q_{\text{mat}}^{-1}$ .  $Q_{\text{rad}}$  is its radiative quality factor, which represents coupling to normally incident radiation, and is designed to be sufficiently low (~10–20) to prevent self-oscillation of the metasurface.  $Q_{\text{mat}}=\omega_0 n/\Gamma c(g_{tr}-g)$  is the material quality factor, where  $n$  is the refractive index of the QC-material,  $c$  is the speed of light,  $g_{tr}$  is the transparency gain which represents material losses (metallic and semiconductor), and  $\Gamma$  is an effective confinement factor of the metasurface mode to the QC-active material. At the central frequency  $\omega_0$ , using a straightforward transmission line model (see supplemental section S1), the peak reflectance from the metasurface can be written as  $R=\left(Q_{\text{rad}}-Q_{\text{mat}}\right)^2/\left(Q_{\text{rad}}+Q_{\text{mat}}\right)^2$ . Provided  $Q_{\text{rad}} \ll |Q_{\text{mat}}|$ , we can approximate  $R \approx e^{\xi(g-g_{tr})}$ , where  $\xi$  is an effective interaction length approximated by  $\xi=4\Gamma c Q_{\text{rad}}/\omega_0$ . In principle, it is straightforward to upscale the central frequency of a metasurface by linearly downscaling all dimensions ( $\Lambda$ ,  $w$ , and  $h$ ). However, while  $Q_{\text{rad}}$  and  $\Gamma$  remain constant during scaling,  $Q_{\text{mat}}$  does not due to the  $\omega_0^{-1}$  dependence of  $\xi$ , which leads to reduced metasurface reflectance. Furthermore, downscaling the height  $h$  of the ridge leads to increased metal losses (i.e. higher  $g_{tr}$ ), but if  $h$  is not downscaled, larger radiative losses and lower  $\Gamma$  reduce the reflectance even more. Use of the patch metasurface counters these effects – it exhibits a larger radiative quality factor

This is the author's peer reviewed, accepted manuscript. However, the online version of record will be different from this version once it has been copyedited and typeset.

PLEASE CITE THIS ARTICLE AS DOI: 10.1063/5.0008867

( $Q_{\text{rad}} \approx 20$ ), and field confinement  $\Gamma$ , both of which increase the value of  $\xi$  and the corresponding metasurface reflectance. As a result, the patches are characterized by a strong field enhancement within, as incident power is collected from an area much larger than the physical patch size.<sup>17</sup> Fig. 1(a) compares the reflectance values for optimized ridge and patch based metasurfaces assuming a fixed 10  $\mu\text{m}$  thick active region at 4.7 THz. The patch metasurface has a value of  $\xi = 163 \mu\text{m}$ , compared to  $\xi = 92 \mu\text{m}$  for the ridge metasurface. See supplemental section S1 and S2 for further discussion of the reflectance and field enhancement.

The second advantage of the patch metasurface is reduced power dissipation thanks to a smaller fill factor (ratio of the area of QC-gain material to total metasurface area) compared with a ridge-based metasurface. So far, QC-VCSELs have tended to be high-power devices, which is natural because the external cavity acts as a power combining scheme from the many sub-cavities on the metasurface.<sup>8</sup> The downside of a high-power device is that it dissipates considerable heat, which increases demands on the cryocooler used. In some applications, it may be preferable to reduce the power and complexity of the cryocooler even at the cost of reduced THz power. One such application is the development of THz QCLs as local-oscillators for remote balloon- and space-based heterodyne observatories, where limited power and space are available for cooling the QCL.<sup>18,19</sup> An obvious solution is to simply reduce the area of the metasurface which receives current injection, but this results in increased diffraction losses (higher threshold gain). The other possibility is to reduce the fill factor and the power dissipated per unit area. Because the ridge width is approximately set to be one-half of the wavelength within the semiconductor ( $w \approx \lambda_0/2n$ , where  $\lambda_0$  is the free-space wavelength), the primary way to reduce the fill factor  $w/\Lambda$  is to increase  $\Lambda$ . However, the period must be kept smaller than the free-space wavelength to prevent coupling with surface modes or higher diffractive orders. Typically,  $\Lambda \leq 0.8\lambda_0$  is used, which limits the minimum fill factor to about 16%. By using a patch-based metasurface we demonstrate a reduction in fill factor to 4%, thus reducing heat dissipation by 75% without reducing the size of the metasurface. Furthermore, the small patches are more efficiently heat sunk. Simulations indicate an average reduction of temperature by  $\sim 10$  K in cw mode (see supplemental section S3).

Microscope and SEM images of a fabricated patch-based metasurface and an illustration of the cavity are shown in Fig. 2(a), finite element simulations of uniform, infinite patch metasurfaces are shown in Fig. 2(b), and an illustration of the VCSEL cavity is shown in Fig. 2(c). The surface is designed to operate near 4.7 THz (63  $\mu\text{m}$  wavelength, motivated by astrophysical interest in atomic oxygen emitting at 4.744 THz)<sup>20,21</sup> and consists of a 2-D

square array of patch elements spaced with a periodicity close to the free-space wavelength in order to minimize fill factor and maximize radiative quality factor ( $\Lambda = 0.75\lambda_0 = 47\ \mu\text{m}$  in both dimensions). Narrow  $1.5\ \mu\text{m}$  wide ridges are used to electrically bias all patches from a single large wirebonding area at the end of the metasurface. Because there is negligible field overlap with these connecting ridges, a layer of insulating oxide is deposited between the top contact and QC-material to prevent wasted pump power.

In Fig. 2(b), the magnitude and phase of reflection at 4.7 THz is shown as a function of patch width, both with and without applied gain (the peak reflectance vs. gain curve is that in Fig. 1). The patches are coupled to radiation polarized along the width  $w$  of the patches ( $x$ -axis in Fig. 2(b)), while coupling to the orthogonal polarization is shorted by the connecting ridges. In order to minimize fill factor and maximize field enhancement, the length of the patches should be made as short as possible. However, there is a tradeoff (illustrated in Fig. 2(d)), between this and the transparency gain  $g_r$ , which increases as fill factor and patch length decrease. As a compromise, patches that are  $7.5\ \mu\text{m}$  long were selected for experiment, yielding a fill factor of  $\sim 4\%$ .

The widths of the patches are spatially varied to provide a parabolic, focusing phase response from the metasurface (focal length,  $f = 5\ \text{mm}$ ). This helps significantly in reducing diffraction losses given that the output coupler is flat (see supplemental section S4). The patches at the center of the metasurface (peak gain at 4.7 THz) are  $11.45\ \mu\text{m}$  wide, and the width of the patches is varied between  $8\text{--}22\ \mu\text{m}$  as a function of radial distance from the center; this spans a total phase range of  $\sim 6$  radians. Since the needed phase variation is obtained by detuning the patch resonance from the design frequency, this has the side effect of reducing the THz amplification provided by those detuned patches. However, since we have chosen a relatively long effective focal length (i.e. a small phase curvature), and a small enough central bias area, the patch elements within the bias area experience minimal detuning from the resonant gain peak. The range of patch sizes that receive bias is indicated in Fig. 2(b). On the other hand, detuning of the outer, unbiased patch elements helps reduce material losses to the outer portion of the THz beam, making up for lost amplification. One disadvantage of the focusing design is that it is less amenable to broadband frequency tuning as the desired phase curvature is only present at a single frequency. The design principles and tradeoffs of such a focusing metasurface are described in detail in Ref. [2].

Fabrication followed a standard metal-metal waveguide process, as outlined in Ref. <sup>22</sup>, with electron-beam lithography used to define the patch metallization pattern. A patterned  $\text{SiO}_2$  layer between the QC-growth and top

This is the author's peer reviewed, accepted manuscript. However, the online version of record will be different from this version once it has been copyedited and typeset.

PLEASE CITE THIS ARTICLE AS DOI: 10.1063/5.0008867

metal contact was used to selectively bias the desired patches but not the connecting elements, unbiased patches, or wire bonding areas. The active region is a  $10\text{ }\mu\text{m}$  thick  $\text{Al}_{0.15}\text{Ga}_{0.85}\text{As}/\text{GaAs}$  heterostructures and is based on the hybrid active region design first published in Ref. <sup>23</sup>, but modified to operate near 4.7 THz (grown at Sandia National Laboratories, wafer VB1010). Starting from the injection barrier, the layer thicknesses in Å are **51/96/14/116/35/90/37/172** (barrier layers are bold). The central 88 Å of the underlined well is Si-doped at  $5\times 10^{16}\text{ cm}^{-3}$ . The total area of the metasurface is  $1.75 \times 1.75\text{ mm}^2$ , but only a central circular area of the metasurface is biased, in order to preferentially pump the fundamental Gaussian external cavity mode.

Experimental results from VECSELs assembled with two different metasurfaces are shown in Fig. 3. The metasurfaces are identical with the exception of different bias are diameters, 1 mm (metasurface 1) and 0.75 mm (metasurface 2) shown in Fig. 3(a) and (b) respectively. The external cavity of the VECSEL is built within the cryostat and aligned before cooling down using the same setup and procedure described in Ref. <sup>3</sup>. Each metasurface was tested with two different output couplers: one with high reflectance ( $\text{OC1} > 97\%$ ) to minimize threshold gain and maximize temperature performance, and one with lower reflectance ( $\text{OC2} \approx 90\%$ ) to maximize power and efficiency. VECSELs constructed with OC1 were tested at 77 K, while VECSELs constructed with OC2 were tested at 4 K and 20 K. The output couplers are made by evaporating metal meshes onto z-cut crystal quartz substrates (see supplementary Fig. S5 for details) and are polarization independent. All measurements were performed in continuous wave (cw) mode (dc electrical bias), see supplemental section S6 for comparison to pulsed results. Measurement results of a conventional metal-metal waveguide QC-laser are shown in supplementary Fig. S7.

Operating at 77 K with OC1, up to 0.8 mW of power is measured with metasurface 1 (0.06% wall-plug efficiency (WPE)), and up to 0.25 mW of power is measured with metasurface 2 (0.03% WPE). Power vs. current ( $P$ - $I$ ) curves were measured with a pyroelectric detector, and absolute power levels were measured using a calibrated thermopile. Power values are corrected for 60% transmission through the 3 mm HDPE cryostat window (see supplemental Fig. S8). The device lased single-mode at  $\sim 4.57$  THz throughout the bias range with both output couplers, slightly lower than the target of 4.7 THz. This is due to lithographic error, with SEM measurements indicating actual feature sizes were 200 nm wider and longer than design, lowering the resonant frequency of the patches by  $\sim 100$  GHz. At this frequency, the output couplers are measured to have 2.5% and 10% transmittance for OC1 and OC2 respectively. Metasurface 1 was tested with a 4 mm long external cavity, while metasurface 2 was

This is the author's peer reviewed, accepted manuscript. However, the online version of record will be different from this version once it has been copyedited and typeset.

PLEASE CITE THIS ARTICLE AS DOI: 10.1063/5.0008867

tested with a shorter 2.5 mm cavity. Shorter external cavities allow for a smaller beam waist because the reduced diffraction loss counteracts the larger divergence of a small beam (see discussion in supplement of Ref. [3]). The smaller beam waist means the mode is better confined to the smaller bias diameter of metasurface 2. Despite the shorter cavity, metasurface 2 showed a significant increase in threshold current density compared to metasurface 1. This difference emphasizes the fact that reducing fill factor is preferable to reducing the size of the metasurface. Maximum cw operating temperature was  $\sim$ 90 K for metasurface 1, and  $\sim$ 80 K for metasurface 2 (see supplemental Fig. S9 for more details on temperature data).

Operating at 4 K with OC2, 6.6 mW of continuous wave power is measured with metasurface 1 (0.67% WPE), and 3.5 mW of power is measured from metasurface 2 when operating at  $\sim$ 20 K (0.5% WPE). The device consistently lased at  $\sim$ 4.56 THz. Both metasurfaces were tested with 2 mm cavities to minimize threshold gain. Maximum operating temperature for both metasurfaces was less than 70 K. Beam patterns from the two metasurfaces are narrow and circular with a divergence angle of  $\sim$ 5°. Some distortion is observed in the central portion of the beam, which may be associated with flaws or interference effects in the cryostat window or output coupler.

In conclusion, a THz QC-VECSEL is presented where the dissipated power is reduced by  $\sim$ 75% compared to previous demonstrations without significantly impacting the threshold gain, efficiency, or beam quality. The smallest device consumes 0.63 W of power while still producing  $>3$  mW of THz power at 4 K (corrected for cryostat window transmission). These levels of continuous-wave power and efficiency are higher than other cw THz QC-lasers reported to operate above 4.5 THz<sup>19,24,25</sup>, and are comparable to some of the smallest 3<sup>rd</sup>-order distributed feedback devices.<sup>26,27</sup> Several novel approaches to microcavity THz QCLs have yielded very small devices<sup>28,29</sup>, but to fully evaluate the applicability of any solution, matters such as power, beam pattern, and frequency control must all be considered. Further reductions in the dissipated power of the QC-VECSEL may be achieved by using very short external cavities and smaller diameter metasurfaces (a metasurface with a 500  $\mu$ m bias diameter was demonstrated in Ref. 3). Alternatively, focusing optics could be used in the external cavity, rather than on the QC metasurface. By placing a uniform metasurface at the focus of a focusing metasurface output coupler, the metasurface *can* be made smaller; this will require more careful external cavity design. Additionally, using a lower bias bound-to-continuum design may have the benefit of further reducing power consumption.<sup>30</sup> Finally, perhaps the ultimate limit for low power dissipation would be to use metasurfaces based on LC "circuit" type THz resonators, although the benefits of

This is the author's peer reviewed, accepted manuscript. However, the online version of record will be different from this version once it has been copyedited and typeset.

PLEASE CITE THIS ARTICLE AS DOI: 10.1063/5.0008867

this approach would have to be carefully balanced against the increased metallic losses incurred in these deep subwavelength structures.<sup>31-33</sup>

#### Supplementary Material

See supplementary material for details on the analytical model of the metasurface, FEM simulations of the metasurface's thermal properties, computational modeling of the external cavity diffraction losses, output coupler transmission measurements, pulsed measurements of the QC-VECSEL, temperature performance of the QC-VECSEL, and measurements of a single metal-metal waveguide ridge device.

#### Acknowledgements

Microfabrication was performed at the UCLA Nanoelectronics Research Facility, electron beam lithography was performed at the California NanoSystems Institute (CNSI) at UCLA, and wire bonding was performed at the UCLA Center for High Frequency Electronics. This work was performed, in part, at the Center for Integrated Nanotechnologies, an Office of Science User Facility operated for the U.S. Department of Energy (DOE) Office of Science. Sandia National Laboratories is a multimission laboratory managed and operated by National Technology and Engineering Solution of Sandia, LLC., a wholly owned subsidiary of Honeywell International, Inc., for the U.S. Department of Energy's National Nuclear Security Administration under contract DE-NA-0003525. Partial funding was provided by the National Science Foundation (1407711, 1711892) and National Aeronautics and Space Administration (NNX16AC73G, 80NSSC19K0700).

#### Data Availability

The data that supports the findings of this study are available within the article [and its supplementary material].

#### REFERENCES

- <sup>1</sup> L. Y. Xu, C. A. Curwen, P. W. C. Hon, Q. S. Chen, T. Itoh, and B. S. Williams, *Appl. Phys. Lett.* **107**, 221105 (2015).
- <sup>2</sup> L. Y. Xu, D. G. Chen, T. Itoh, J. L. Reno, and B. S. Williams, *Opt. Express* **24**, 24117 (2016).
- <sup>3</sup> C. A. Curwen, J. L. Reno, and B. S. Williams, *Nat. Photon.* **13**, 855 (2019).
- <sup>4</sup> L. Y. Xu, D. G. Chen, C. A. Curwen, M. Memarian, J. L. Reno, T. Itoh, and B. S. Williams, *Optica* **4**, 468 (2017).
- <sup>5</sup> L. Y. Xu, C. A. Curwen, D. G. Chen, J. L. Reno, T. Itoh, and B. S. Williams, *IEEE J. Sel. Top. Quantum Electron.* **23**, 1200512 (2017).

This is the author's peer reviewed, accepted manuscript. However, the online version of record will be different from this version once it has been copyedited and typeset.

PLEASE CITE THIS ARTICLE AS DOI: 10.1063/5.0008867

<sup>6</sup> P. W. C. Hon, A. A. Tavallaei, Q. S. Chen, B. S. Williams, and T. Itoh, *IEEE Trans. Terahertz Sci. Technol.* **2** (2012).

<sup>7</sup> L. Y. Xu, C. A. Curwen, J. L. Reno, and B. S. Williams, *Appl. Phys. Lett.* **111**, 101101 (2017).

<sup>8</sup> C. A. Curwen, J. L. Reno, and B. S. Williams, *Appl. Phys. Lett.* **113**, 011104 (2018).

<sup>9</sup> D. M. Pozar and T. A. Metzler, *Electron. Lett.* **29**, 657 (1993).

<sup>10</sup> P. C. Hon, Ph.D. Thesis, University of California, Los Angeles, 2013.

<sup>11</sup> C. Ciuti, G. Bastard, and I. Carusotto, *Phys Rev B* **72** (2005).

<sup>12</sup> D. Palaferri, Y. Todorov, Y. N. Chen, J. Madeo, A. Vasanelli, L. H. Li, A. G. Davies, E. H. Linfield, and C. Sirtori, *Appl. Phys. Lett.* **106**, 161102 (2015).

<sup>13</sup> D. Palaferri, Y. Todorov, A. Bigioli, A. Mottaghizadeh, D. Gacemi, A. Calabrese, A. Vasanelli, L. H. Li, A. G. Davies, E. H. Linfield, F. Kapsalidis, M. Beck, J. Faist, and C. Sirtori, *Nature* **556** (2018).

<sup>14</sup> Y. Todorov, L. Tosetto, A. Delteil, A. Vasanelli, C. Sirtori, A. M. Andrews, and G. Strasser, *Phys Rev B* **86**, 125314 (2012).

<sup>15</sup> J. Madeo, Y. Todorov, A. Gilman, G. Frucci, L. H. Li, A. G. Davies, E. H. Linfield, C. Sirtori, and K. M. Dani, *Appl. Phys. Lett.* **109**, 141103 (2016).

<sup>16</sup> J. Perez-Urquiza, J. Madeo, Y. Todorov, L. Li, A. G. Davies, E. Linfield, C. Sirtori, and K. M. Dani, 2019 44th International Conference on Infrared, Millimeter, and Terahertz Waves (IRMMW-THz) (2019).

<sup>17</sup> D. Palaferri, Y. Todorov, A. Mottaghizadeh, G. Frucci, G. Biasiol, and C. Sirtori, *New J. Phys.* **18**, 113016 (2016).

<sup>18</sup> H. Richter, M. Wienold, L. Schrottke, K. Biermann, H. T. Grahn, and H. W. Hubers, *IEEE Trans. Terahertz Sci. Technol.* **5**, 539 (2015).

<sup>19</sup> D. J. Hayton, J. L. Kloosterman, Y. Ren, T. Y. Kao, J. R. Gao, T. M. Klapwijk, Q. Hu, C. K. Walker, and J. L. Reno, *Proc. SPIE* **9153**, 91531R (2014).

<sup>20</sup> G. L. Pilbratt, J. R. Riedinger, T. Passvogel, G. Crone, D. Doyle, U. Gageur, A. M. Heras, C. Jewell, L. Metcalfe, S. Ott, and M. Schmidt, *Astron. Astrophys.* **518**, L1 (2010).

<sup>21</sup> S. Leurini, F. Wyrowski, H. Wiesemeyer, A. Gusdorf, R. Gusten, K. M. Menten, M. Gerin, F. Levrier, H. W. Hubers, K. Jacobs, O. Ricken, and H. Richter, *Astron. Astrophys.* **584**, A70 (2015).

<sup>22</sup> B. S. Williams, S. Kumar, Q. Hu, and J. L. Reno, *Opt. Express* **13**, 3331 (2005).

<sup>23</sup> M. I. Amanti, G. Scalari, R. Terazzi, M. Fischer, M. Beck, J. Faist, A. Rudra, P. Gallo, and E. Kapon, *New J. Phys.* **11**, 125022 (2009).

<sup>24</sup> L. Schrottke, X. Lu, B. Roben, K. Biermann, T. Hagelschuer, M. Wiedner, H. W. Hubers, M. Hannemann, J.-P. H. Van Helden, J. Ropcke, and H. T. Grahn, *IEEE Trans. Terahertz Sci. Technol.* **10**, 113 (2020).

<sup>25</sup> L. Bosco, C. Bonzon, K. Ohtani, M. Justen, M. Beck, and J. Faist, *Appl. Phys. Lett.* **109**, 201103 (2016).

<sup>26</sup> M. Wienold, B. Roben, L. Schrottke, R. Sharma, A. Tahraoui, K. Biermann, and H. T. Grahn, *Opt. Express* **22**, 3334 (2014).

<sup>27</sup> F. Joint, G. Gay, P. B. Vigneron, T. Vacelet, S. Pirotta, R. Lefevre, Y. Jin, L. H. Li, A. G. Davies, E. H. Linfield, Y. Delorme, and R. Colombelli, *Appl. Phys. Lett.* **115**, 231104 (2019).

<sup>28</sup> Y. Chassagneux, J. Palomo, R. Colombelli, S. Dhillon, C. Sirtori, H. Beere, J. Alton, and D. Ritchie, *Appl. Phys. Lett.* **90**, 091113 (2007).

<sup>29</sup> L. Masini, A. Pitanti, L. Baldacci, M. S. Vitiello, R. Degl'Innocenti, H. E. Beere, D. A. Ritchie, and A. Tredicucci, *Light-Sci Appl* **6**, e17054 (2017).

<sup>30</sup> M. Wienold, L. Schrottke, M. Giehler, R. Hey, W. Anders, and H. T. Grahn, *Electron. Lett.* **45**, 1030 (2009).

<sup>31</sup> C. Walther, G. Scalari, M. I. Amanti, M. Beck, and J. Faist, *Science* **327**, 1495 (2010).

<sup>32</sup> E. Strupiechonski, G. Xu, P. Cavalie, N. Isac, S. Dhillon, J. Tignon, G. Beaudoin, I. Sagnes, A. Degiron, and R. Colombelli, *Phys Rev B* **87**, 041408 (2013).

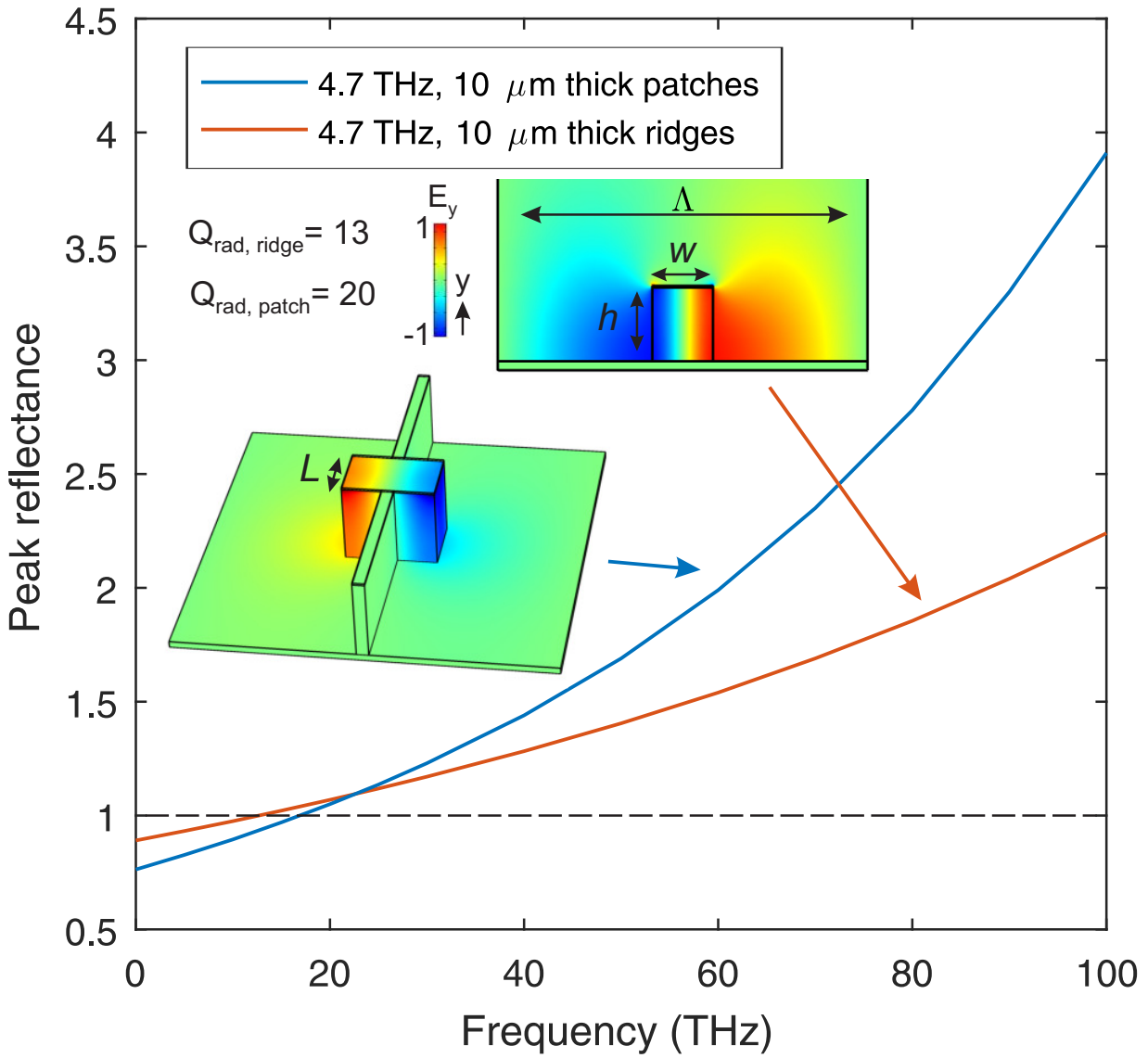
<sup>33</sup> M. Jeannin, G. M. Nesurini, S. Suffit, D. Gacemi, A. Vasanelli, L. H. Li, A. G. Davies, E. Linfield, C. Sirtori, and Y. Todorov, *ACS Photonics* **6**, 1207 (2019).

#### Figure captions

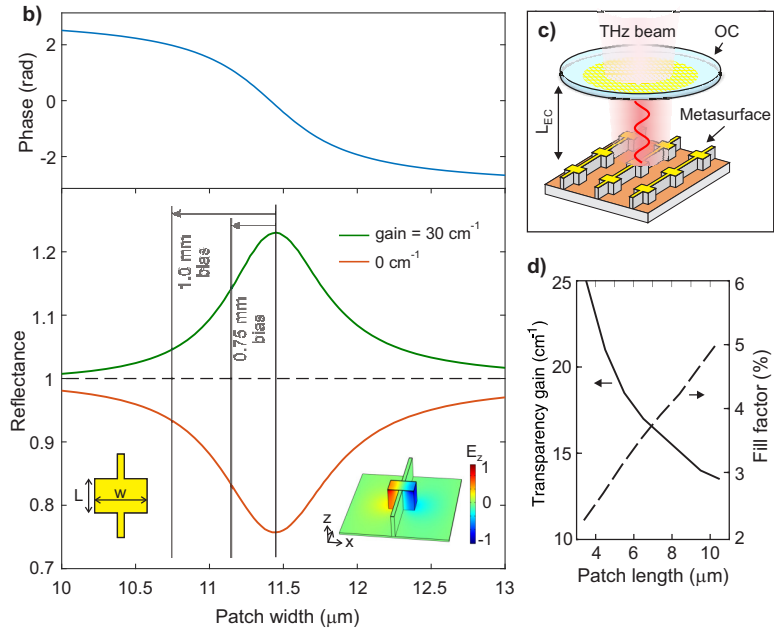
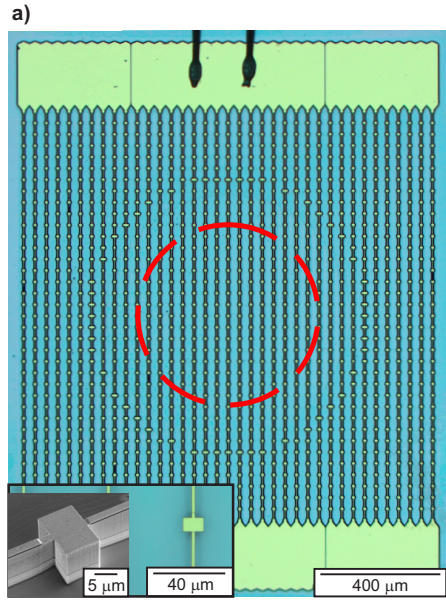
**FIG. 1.** (a) Simulated peak reflectance for a ridge-based ( $\Lambda = 50 \mu\text{m}$ ,  $w = 8.3 \mu\text{m}$ ) and patch-based ( $\Lambda = 47 \mu\text{m}$ ,  $w = 11.45 \mu\text{m}$ ,  $L = 7.5 \mu\text{m}$ ) metasurface design for a  $10 \mu\text{m}$  thick 4.7 THz active region. Insets show field distribution for the two cases (note: relative strength of fields between the patch and ridge are not to scale).

**FIG. 2.** (a) Microscope images of the metasurface. A  $0.75 \text{ mm}$  bias diameter is indicated by the dashed red line. Inset shows microscope and SEM image of a single patch. (b) Finite element electromagnetic simulations of the reflection magnitude and phase at 4.7 THz of a uniform patch-based metasurface as a function of the width of the patch  $w$  (period  $\Lambda=47 \mu\text{m}$ ). The range of patch widths  $w$  across the non-uniform metasurfaces that receive electrical bias is indicated. (c) Illustration of the VECSEL cavity. (d) Effect of patch length  $L$  on the transparency gain  $g_{tr}$  and fill factor of the metasurface.

**FIG. 3.** (a) Continuous-wave  $P$ - $I$ - $V$  data (power corrected for cryostat window transmission) from  $1.75 \times 1.75 \text{ mm}^2$  VECSEL with two different output couplers and two different metasurfaces with (a)  $1 \text{ mm}$  and (b)  $0.75 \text{ mm}$  diameter bias areas in the center. Maximum power and efficiency are achieved with the high transmittance output coupler (OC 2). Maximum temperature performance is achieved with the low transmittance output coupler (OC 1). Spectra and beam patterns are also presented.



This is the author's peer reviewed, accepted manuscript. However, the online version of record will be different from this version once it has been copyedited and typeset.  
PLEASE CITE THIS ARTICLE AS DOI: 10.1063/5.0008867



This is the author's peer reviewed, accepted manuscript. However, the online version of record will be different from this version once it has been copyedited and typeset.

PLEASE CITE THIS ARTICLE AS DOI: 10.1063/5.0008867

